Surface Hardening of a Gray Cast Iron Used for a Diesel Engine Cylinder Block Using High-Energy Electron Beam Irradiation

SEONG-HUN CHOO, SUNGHAK LEE, and SOON-JU KWON

This study investigates the effects of high-energy electron-beam (1.4 MeV) irradiation on surface hardening and microstructural modification in a gray cast iron currently used for a diesel engine cylinder block. The gray cast-iron samples were irradiated in air using an electron accelerator. Afterward, their microstructure, hardness, and wear properties were examined. The original microstructure, which contained graphite flakes in a pearlitic matrix, was changed to martensite, ledeburite, and retained austenite, along with complete or partial dissolution of the graphite. This microstructural modification occurred only when the surface was irradiated with an input-energy density over 1.1 kJ/cm^2, and it greatly improved the surface hardness and wear resistance. In order to investigate the complex microstructures, thermal analysis and simulation testing were also carried out. The results indicated that the irradiated surface was heated to the austenite-temperature region and then quenched to room temperature, which was enough to obtain surface hardening through martensitic transformation. The thermal analysis results matched well with the microstructures of the thermally simulated samples.

I. INTRODUCTION

SINCE gray cast iron contains a high percentage of flake graphite, it has special properties such as excellent machinability, the ability to resist galling with restricted lubricant, and excellent vibration damping.[1–4] Cylinder blocks and heads are some of the ways in which the damping capacity of gray cast iron is utilized. As the demand for high performance and durability in automobiles has recently soared, strenuous efforts have been made to improve the wear resistance of engine parts by hardening their surfaces. Notably, the surface modification of cast irons by high-energy beams such as the laser beam and electron beam has been studied extensively by many investigators.[5–11] Since an electron beam has an energy range from 50 to 200 keV, it usually requires a vacuum chamber, which is one of the many limitations of an electron beam as compared to the laser beam.[11,12,13]

Recently, a high-energy electron-beam (energy range: 0.5 to 1.5 MeV) irradiation technique, which can be extracted into air, has been developed.[14,15,16] A high-energy electron beam can penetrate up to several tens of centimeters of air. Because the depth of the hardened surface layer is proportional to the electron penetration depth, a layer depth of about 1 mm can be hardened by a high-energy electron beam without surface melting, which is almost impossible by the laser technique. Furthermore, many overlappings are not needed to harden a broad area, because the scanning width of an electron beam can be easily controlled up to several tens of centimeters by changing the magnetic field. Blacking is not necessary in electron-beam surface hardening. In spite of these advantages, little attempt has been made to apply it to industrial practice.

The present study aims to improve the durability of automotive parts by applying high-energy electron-beam irradiation to the gray cast iron used for an automotive diesel engine cylinder block and, thereby, modifying its surface structure. To attain the maximum hardened depth and the peak hardness without surface melting, it was essential to establish the optimum irradiation conditions. Surface hardness and wear properties can be enhanced by the phase transformation from pearlite to martensite, while flake graphites remain and play their own distinctive roles.[2,3] The surface hardening mechanism was clarified by investigation of the microstructural modification and the phase transformation both before and after irradiation. Correlations between process parameters, microstructures, and surface properties were also investigated. Furthermore, thermal analysis was conducted to calculate the temperature distribution, including peak temperature, cooling rate, and irradiation depth. To verify the applicability of this model, a thermal simulation test was conducted, and the results were analyzed in comparison to those of actual irradiation.

II. EXPERIMENTAL PROCEDURE

A. *Material*

The material used in the present study was the gray cast iron (FCH2D) commercialized for a diesel engine cylinder block and was a product finished in its final form through casting. Its chemical composition is Fe-3.54C-2.21Si-0.67Mn-0.025Cr-0.013Cu-0.056P-0.031S (wt pct). The sample was about 19-mm thick, the maximum possible thickness that can be obtained from the cylinder block. It was machined to a size of 30 × 30 × 19 mm to prepare wear-test specimens.

SEONG-HUN CHOO, Research Assistant, and SUNGHAK LEE, Professor, are with the Center for Advanced Aerospace Materials, Pohang University of Science and Technology, Pohang, 790-784 Korea. SOON-JU KWON, Associate Professor, is with the Department of Materials Science and Engineering, Pohang University of Science and Technology, Pohang, 790-784 Korea.

Manuscript submitted September 30, 1997.

B. *Irradiation with a High-Energy Electron Beam*

The irradiation with a high-energy electron beam was conducted at the Budker Institute of Nuclear Physics (Novosibirsk, Russia) using an electron accelerator (Model ELV-6). The energy of this electron accelerator ranges from 0.5 to 1.5 MeV, and the maximum beam current and power are 70 mA and 100 kW, respectively. The irradiation conditions are determined by process parameters such as the beam current and beam traveling speed and by material constants such as the density, thermal conductivity, and thermal diffusivity. The electron beam size (d) varies with the distance (h) from the final diaphragm to the sample surface and is related experimentally to the following equation, in the case of the ELV-6 electron beam accelerator:[14]

$$d = 0.1 + 0.055h + 0.0075 \sqrt{\frac{1.4\ (MeV)}{U\ (MeV)}}\, h^2 \qquad [1]$$

Here, the electron beam size is calculated to be 1.02 cm, because the electron energy (U) is 1.4 MeV and the value of h is 8 cm. The beam-current density has a Gaussian distribution, showing an exponential decrease as it gets farther away from the central axis of the beam. If the maximum current density at the central axis is J_0, the beam current density ($J(r)$) along the distance from the central axis (r) can be expressed by the following equation:[17]

$$J(r) = J_0 \exp\left(-\frac{r^2}{r_b^2}\right) \qquad [2]$$

where r_b is the beam radius ($d/2$). If scanning is carried out with the beam fixed, the heat input irradiated on the sample surface becomes inhomogeneous due to the difference in current density between the central and the edge regions. In this study, to expand the beam-treated area while avoiding the inhomogeneity of heat input, the beam was scanned at a deflection angle of about ± 10 deg in the horizontal direction.

The electron range (S), *i.e.*, the penetration depth of the electrons, varies, as in the following formula, in the case of an electron-beam energy of over 1 MeV:[18,19]

$$S \approx \frac{1}{\rho}\,(5.1 \times 10^{-7}\, U - 0.26) \qquad [3]$$

Because the density (ρ) of the gray cast iron is about 7.04 g/cm^3, the electron range is calculated to be about 640 μm. The process conditions were calculated in the aforementioned manner, the results of which are listed in Table I, together with irradiation conditions and material constants.[1] In the present study, the input-energy density (W), *i.e.*, the input energy per unit area, was varied, with all other process parameters being fixed at the optimum conditions. The beam scanning width, which can be adjusted by varying the electromagnetic field, was fixed at 3.2 cm, a little larger than the sample size, so that the sample surface could be sufficiently irradiated. When the beam traveling speed (v) and the scanning width (l) are decided, the input-energy density is calculated in proportion to the beam power as follows:[14]

$$W = \frac{(1 - f)P}{vl} \qquad [4]$$

where f is the electron reflectivity from the sample surface, and P is the beam power. The reflectivity varies with the electron energy and the atomic number. When an electron beam ranging from 1 to 2 MeV is irradiated on iron or steel, the reflectivity is about 40 pct.[20,21] For convenience, the irradiated samples were named samples A through E, respectively, depending on the beam current used. The calculated values of input-energy density are listed in Table II.

C. *Microstructural Analysis and Hardness Testing*

The central region of the irradiated samples was sectioned perpendicular to the irradiation direction. To minimize the loss and deformation to the samples, they were sectioned by an electrodischarge machine. They were polished, etched in nital, and examined by an optical microscope. Quantitative analyses of retained austenite, cementite carbides, martensite, and ferrite were done using Mössbauer spectroscopy. Because the Mössbauer spectroscopy provides information on the local environment of iron atoms only,[22] flake graphites cannot be analyzed. A 20mCi Co^{57} gamma ray was used as a source, and disc specimens of about 10 mm in diameter and about 100 μm in thickness were obtained from the irradiated surface layer. Also, the microhardness of the matrix only, excluding flake graphites, was measured along the depth from the surface by a Vickers harness tester, under a load of 50 g.

D. *Friction Wear Test*

The wear test was conducted using a friction wear tester (Model EFM-III-EN/F, Orientec Co.) of ring-on-disc type. An SUS 420 J2 stainless steel was used for the upper ring, which had a 25.6 mm o.d. and a 20 mm i.d. The lower disc, measuring 30 $\times$ 30 $\times$ 5 mm, was prepared from the irradiated surface. Wear arises from friction with the upper ring in a pressurized state while the lower disc rotates. The wear test was conducted for 5 hours at room temperature under a 50 kgf applied load, a 67 rpm rotating speed, and a 1500 m sliding distance, without using any lubricants. Wear resistance was evaluated from the weight loss after testing.

Table I. Irradiation Conditions of High-Energy Electron Beam and Material Constants of the Gray Cast Iron

Process Parameter		Material Constant	
Electron energy	1.4 MeV	thermal diffusivity, k	0.12 cm^2/s
Beam current	4.35 to 8.35 mA		
Beam traveling speed	1 cm/s	thermal conductivity, K	0.502 Watt/cm °C
Beam diameter	1.02 cm		
Scanning width	3.2 cm	electron reflectivity, f	0.4
Distance from diaphragm to specimen	8 cm		
Input energy density, W	1.14 to 2.19 kJ/cm^2	electron range, S	640 μm

Table II. Input Energy Density, Depth of Hardened Layer, and Maximum Hardness of the Gray Cast Iron Samples Irradiated by High-Energy Electron Beam

Sample	A	B	C	D	E
Beam current (mA)	8.35	7.35	6.35	5.35	4.35
Input energy density, W (kW/cm^2)	2.19	1.93	1.67	1.41	1.14
Depth of hardened layer (μm)	2050 (900/850/300)*	700	450	250	0
Maximum hardness (VHN)	860	830	810	790	≈300 (matrix)

*Depths of the melted, the transformed, and the partially transformed regions, respectively.

E. *Thermal Simulation Test*

In order to understand the phase transformation behavior of the irradiated samples, the thermal simulation test was conducted using a dilatometer. The specimens used were a round tubular type of 1-mm thickness, 5-mm o.d., and 10-mm length to achieve fast heating and cooling rates. They were abruptly heated at 100 °C/s, held at the peak temperature (T_p) for the shortest possible time, and then rapidly quenched at 130 °C/s. The T_p was changed in the range from 700 °C to 1160 °C. Here, 1160 °C is the approximate melting temperature of the gray cast iron. After the test, the microstructure was examined by an optical microscope, and the results were compared to those of the actually irradiated samples.

III. RESULTS

A. *Preirradiation Microstructure*

Figures 1(a) and (b) are optical micrographs of the unirradiated gray cast iron. Flake graphites, pores, and MnS particles are observed in the microstructure of the unetched sample, as shown in Figure 1(a). The size and distribution of flake graphites show deviations in the thickness direction, because the cooling rate differs in locations and because graphites float up to the surface during casting. Since all analyses were done at the same location of the surface region, the distribution effect of graphites was not taken into account. Pores are typical casting defects, and a few MnS particles hardly affect the properties of the cast iron.[3] The nital-etched micrograph of Figure 1(b) shows that the matrix of the gray cast iron is mainly composed of pearlite, together with a small amount of eutectic structure of iron and iron phosphide, *viz.*, steadite, as indicated by arrows. These steadites are solidified in the temperature range from 954 °C to 980 °C and are reported as hard and brittle compounds segregated mainly in the interfacial regions of solidification cells.[3,23]

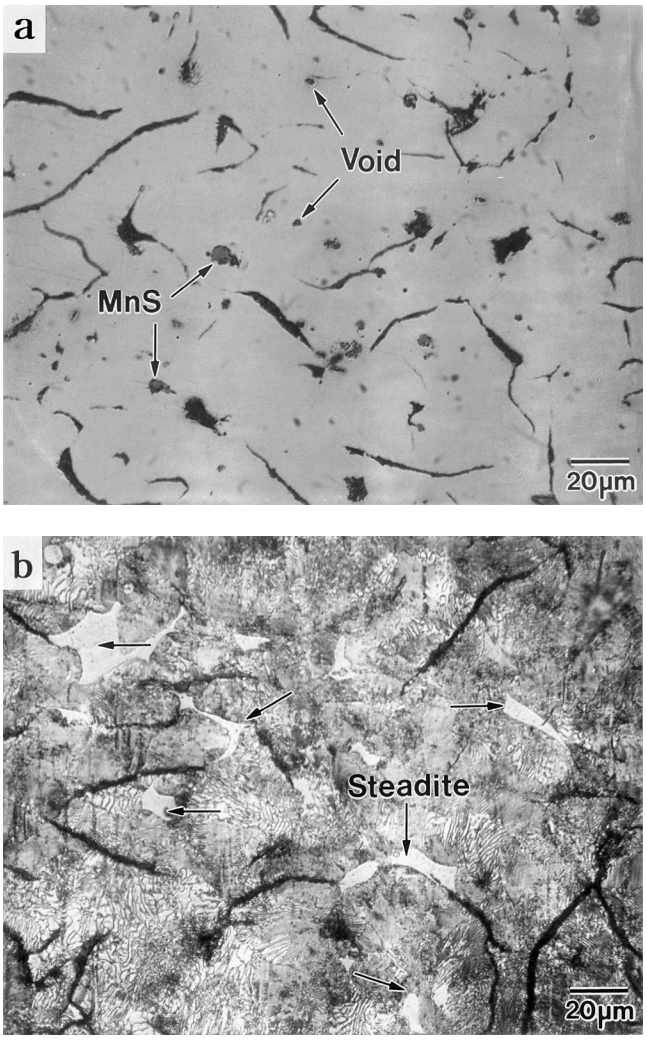

Fig. 1—(*a*) and (*b*) Optical micrographs of the gray cast iron used for a diesel engine cylinder block. (a) and (b) are nonetched and nital-etched microstructures, respectively. Note phosphorus constituent steadites as indicated by arrows in (b).

B. *Postirradiation Microstructure*

Figures 2(a) through (d) are low-magnification optical micrographs which illustrate the microstructural modification as the irradiation condition changes. In sample A, irradiated with an input-energy density of 2.19 kJ/cm^2, the microstructure is modified to the depth of about 2,000 μm, as shown in Figure 2(a). The melted region extends to a depth of 900 μm from the surface. Below the melted region, flake graphites are left almost intact, and only the matrix pearlite structure is transformed as the irradiated thermal energy is transmitted into the interior. Thus, it can be called the transformed region. At the interface between the unaltered and the transformed regions, a heat-affected zone (HAZ) is formed, which does not differ much from the unaltered region, and there is no clear demarcation between the regions. Based on these observations, the microstructure of sample A can be divided into four regions, *i.e.*, the melted region, transformed region, partially transformed region, and unaltered region, as marked by arrows in Figure 2(a).

Figure 2(b) is an optical micrograph of sample B, irradiated with an input-energy intensity of 1.93 kJ/cm^2. Here,

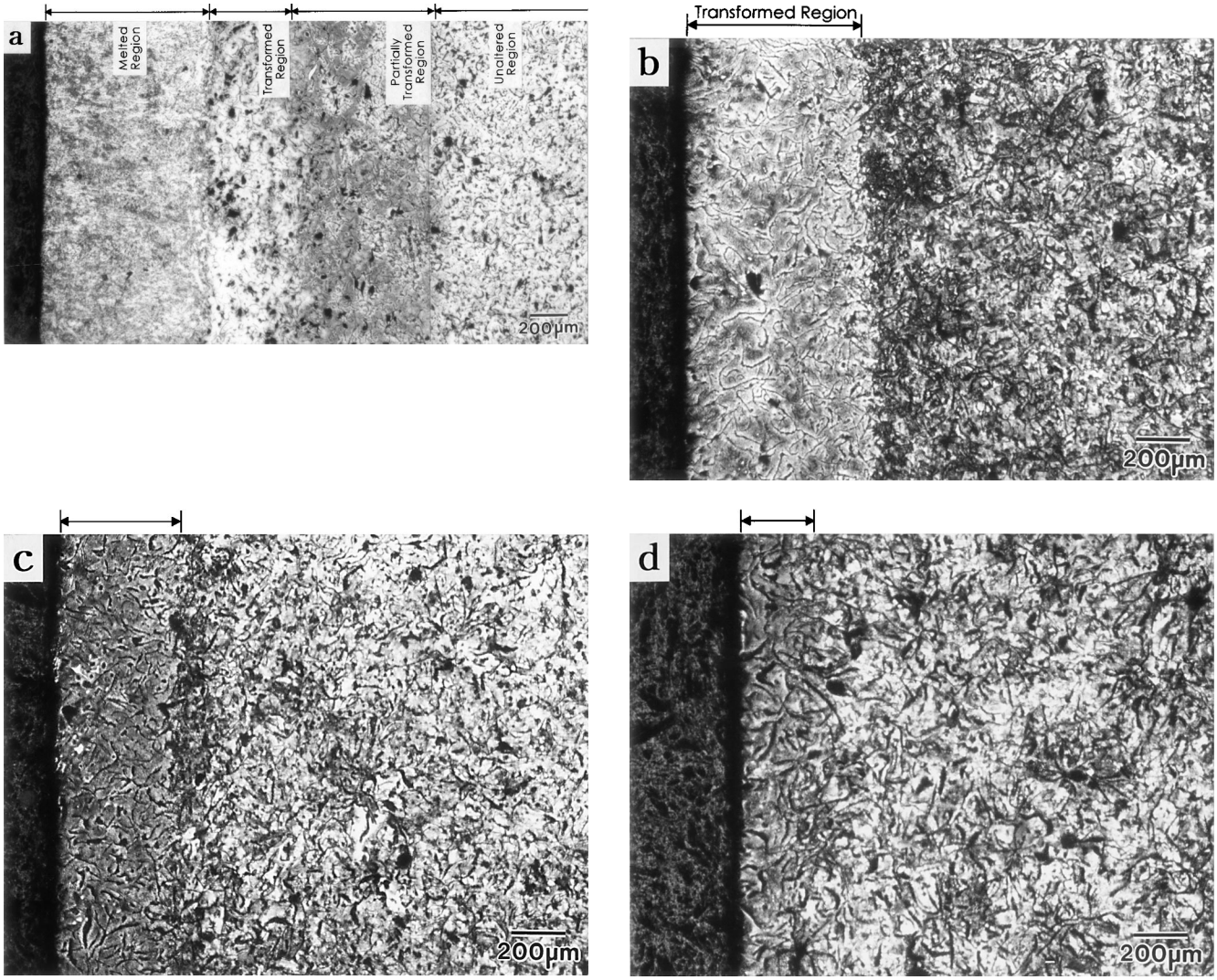

Fig. 2—Optical micrographs of the gray cast iron samples irradiated with high-energy electron beam: (*a*) sample A, (*b*) sample B, (*c*) sample C, and (*d*) sample D.

the melted region is not as visible as it was in sample A, and the transformed region only is formed to a depth of about 700 μm. Samples C and D, irradiated with 1.67 and 1.41 kJ/cm^2, respectively, show similar microstructures to that of sample B (Figures 2(c) and 2(d)), but the depth of the irradiated layer is reduced to about 450 and 250 μm, respectively. In the case of sample E, irradiated with 1.14 kJ/cm^2, there is no sign of microstructural modification. These results indicate that the microstructural modification occurs only when the surface is irradiated with input-energy density over 1.14 kJ/cm^2.

Figures 3(a) through (d) are higher-magnification optical micrographs of sample A. The melted region consists of a dendritic solidification structure (Figure 3(a)). The microstructure of the gray cast iron is modified into one similar to that of a white cast iron *via* the process of melting and rapid solidification. A ledeburite eutectic structure composed of γ + Fe_3C is formed[24] and grows sidewise as well as edgewise, resulting in a typical structure of white cast iron composed of an interdendritic ledeburite eutectic structure.[25] As the temperature was raised above the melting point, the carbon content in the interface between the flake graphites and the matrix reaches a sufficient level (4.3 pct) to cause the eutectic reaction and to form ledeburites. These ledeburites are mostly retained in the final microstructure because of the rapid quenching. However, the matrix is primarily composed of martensite due to the rapid cooling rate, unlike the pearlitic matrix of a typical white cast iron.

Figure 3(b) shows the interfacial area between the melted and the transformed regions. In the transformed region just beneath the interface, the pearlitic matrix is transformed into martensite, with flake graphite remaining. Melting does not occur because the temperature does not rise as high as in the melted region. Austenite is rapidly quenched to transform to martensite, or part of it is retained until room temperature is reached. As a result, coarse plate martensite is observed inside the retained austenite. This plate martensite becomes finer and more densely populated as it gets into the interior, and the fraction of retained austenite tends to be reduced, as shown in Figure 3(c). In the lower part of the transformed region (Figure 3(d)), steadites are observed, as marked by arrows. This indicates that the temperature was not raised high enough to dissolve steadites; thus, this particular region can be called the partially transformed region.

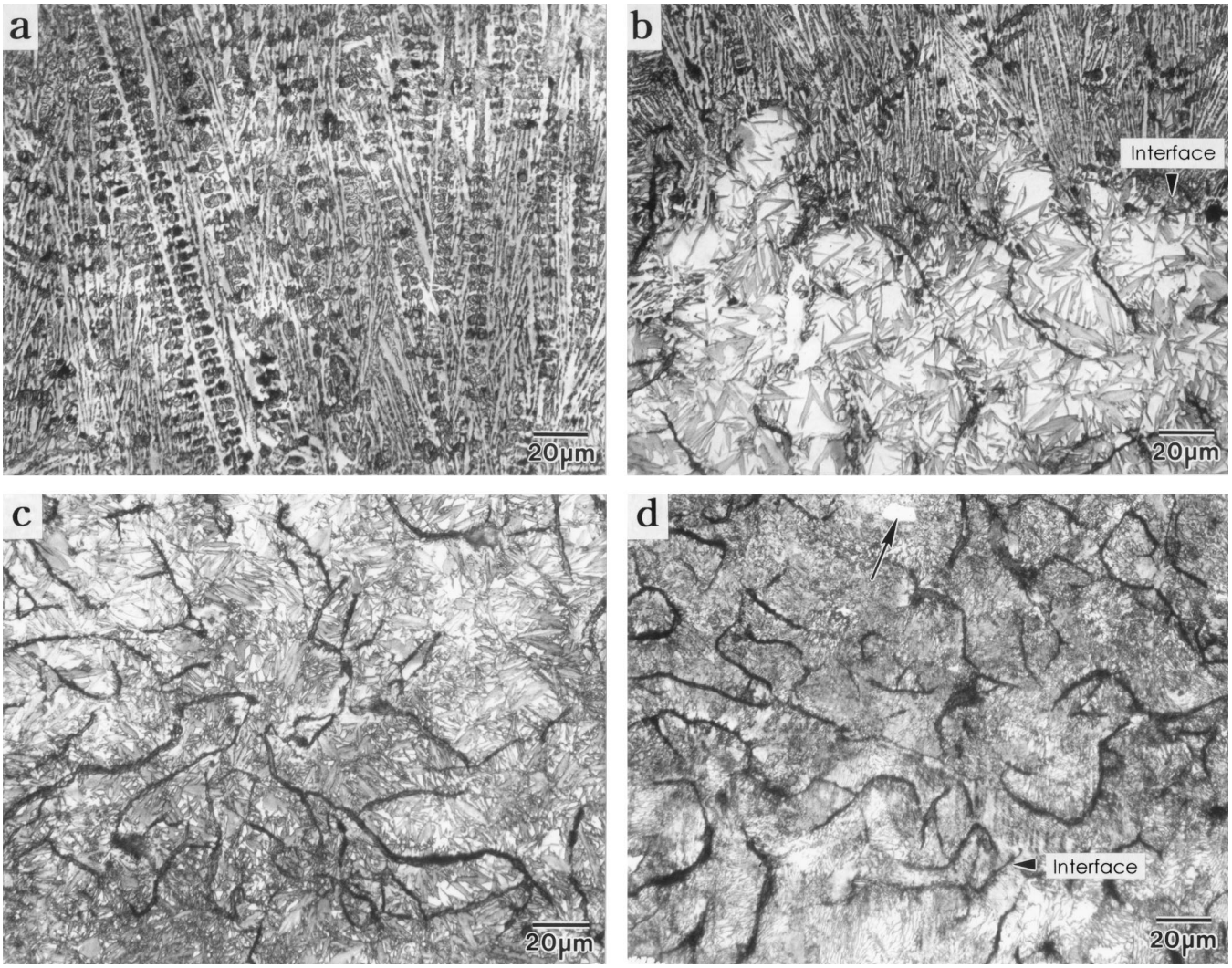

Fig. 3—Optical micrographs of sample A irradiated with highest input energy density, showing (*a*) the melted, (*b*) the melted/transformed interfacial, (*c*) the transformed, and (*d*) the partially transformed regions.

C. *Mössbauer Spectroscopy*

The phases present inside the unaltered, transformed, and melted regions of sample A were quantitatively analyzed by Mössbauer spectroscopy, and the results are shown in Figures 4(a) through (c) and in Table III. The unaltered region is composed of 82 pct ferrite and 18 pct Fe_3C, as can be seen in Figure 4(a), which is consistent with the fact that the matrix is made up of pearlite. Because the gray cast iron contains about 2 pct of Si, ferrite peaks are displayed in three areas, as marked by II, III, and IV in the figure. Peaks II and III are shown by ferrites containing Si, whereas peak IV is shown by pure ferrite. The transformed region consists of 76 pct martensite, 10 pct austenite, and 14 pct Fe_3C carbides (Figure 4(b)). There are four martensite peaks present in the transformed region, among which peaks IV and V are formed by martensite containing Si, while peaks VI and VII are formed by martensite without Si. The melted region is composed of 46 pct martensite, 5 pct austensite, and 49 pct Fe_3C carbides (Figure 4(c)). The number of peaks of martensite is the same (four) as in the transformed region. The melted region consists of a eutectic ledeburite structure made up of carbides, martensite, and a small amount of retained austenite, while the transformed region consists of martensite and retained austenite, corresponding to the microstructures of Figures 3(a) and (c).

D. *Hardness*

Since the most-critical factor affecting wear resistance of the gray cast iron is hardness, Vickers microhardness values of the four irradiated samples were measured along the depth from the surface, and their results are shown in Figures 5(a) and (b). Vickers hardness number (VHN) microhardness values in the melted and the transformed regions of sample A (Figure 5(a)) range from 600 to 850 VHN and show a double to triple increase over the unaltered matrix hardness of about 300 VHN. The hardnesses stay constant at around 800 VHN to the depth of about 900 μm. Where the transformed region starts, the hardness is radically reduced to 600 VHN, gradually rises again up to an 1800 μm depth, where it reaches 850 VHN, and then falls again up to a 2100 μm depth, where the unaltered region appears. These three regions correspond, respectively, to the melted, transformed, and partially transformed regions in Figure 2(a). A low

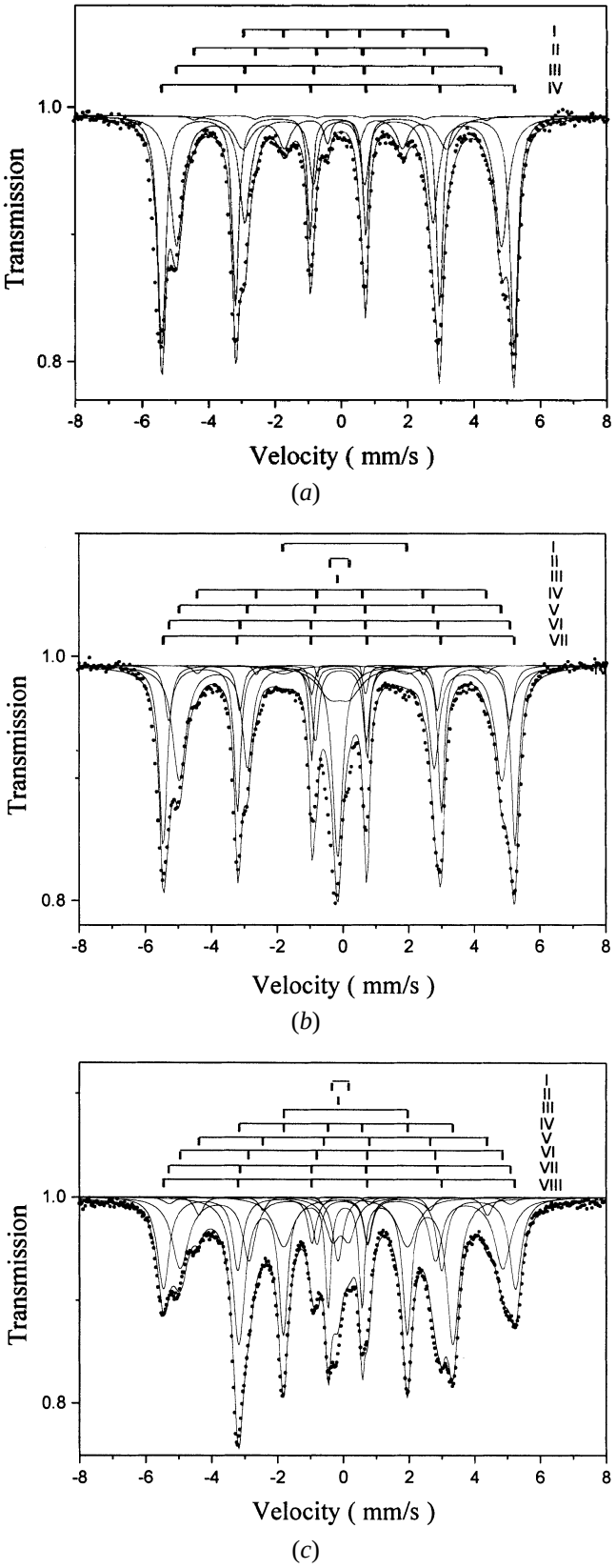

Fig. 4—Mössbauer spectra of (*a*) the unaltered, (*b*) the transformed, and (*c*) the melted regions in sample A.

Table III. Quantitative Results of the Mössbauer Spectroscopy for the Unirradiated and the Irradiated Surface Layers for Sample A without Taking Account of Graphites (Error Range: ± 2 Percent)

Phase	Unaltered Region	Transformed Region	Melted Region
Ferrite	82	—	—
Martensite	—	76	46
Austenite	—	10	5
Fe_3C	18	14	49

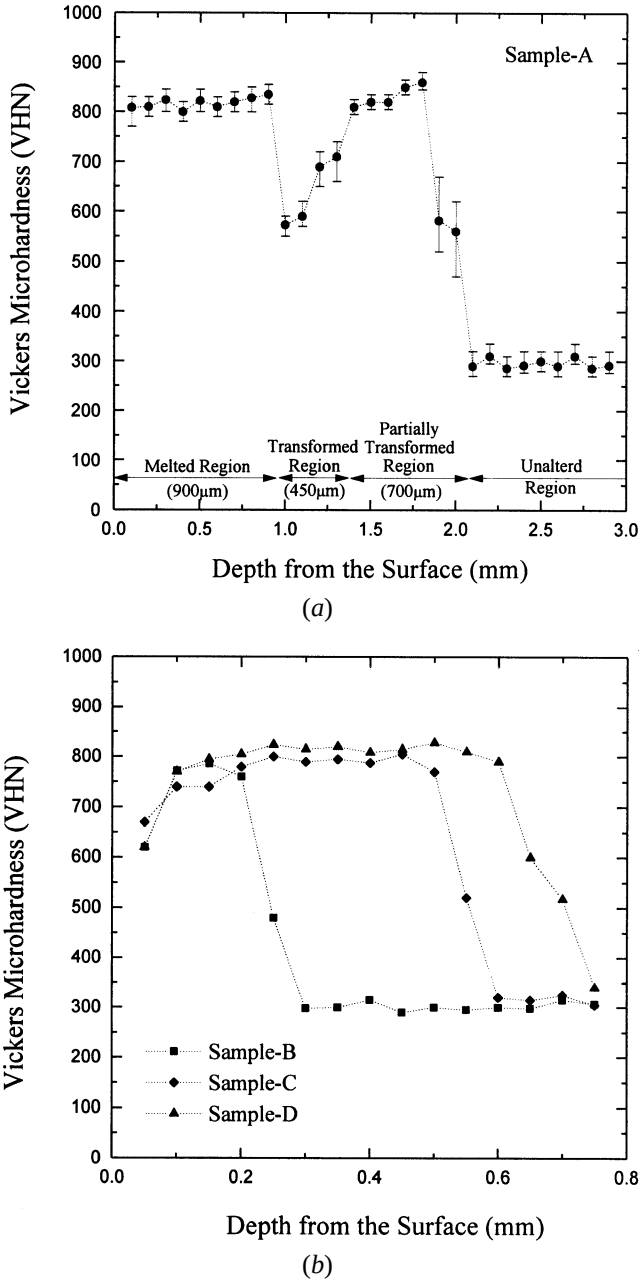

Fig. 5—Vickers microhardness *vs* depth from the irradiated surface of (*a*) sample A and (*b*) sample B through D.

hardness at the start of the transformed region is associated with the extreme formation of retained austenite around coarse plate martensite. The presence of martensite here contributes to a hardness as high as twice that of the matrix harness. In the transformed region, the hardness increases

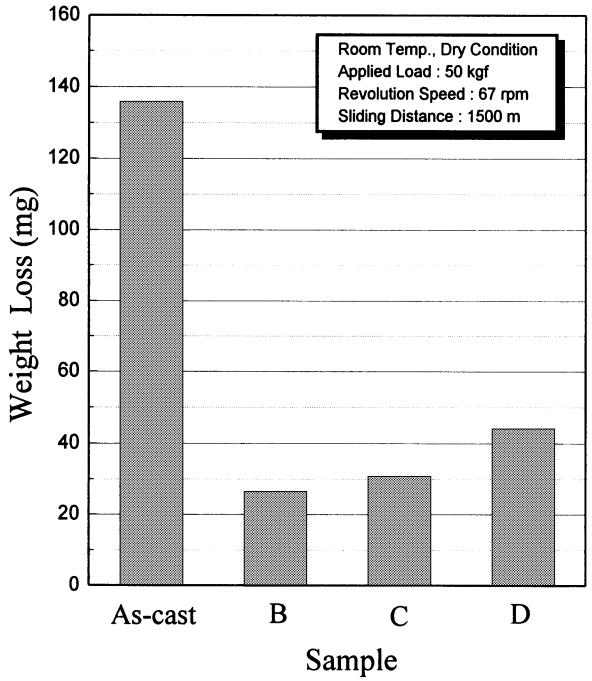

Fig. 6—Friction wear resistance test data for the unirradiated sample and the irradiated samples B through D. Wear resistance was evaluated from the weight loss of the wear specimen after testing.

as it gets into the interior, because of a decreasing amount of retained austenite and of further refinement and densification of plate martensite (Figures 3(b) and (c)). The interval from a 1400 to 2100 μm depth is the partially transformed region (Figure 3(d)), where martensite is transformed partially within cementite lamellae and shows a deviation of hardness dependent on the location. The region beyond 2100 μm in depth is the HAZ, through which the irradiated heat is transferred and which, accordingly, has the same hardness level as in the matrix.

In sample B, the hardness shows an increase from 600 to 800 VHN and is then nearly constant to a depth of 600 μm (Figure 5(b)), corresponding to the transformed region of Figure 2(b). This result might be further evidence that microstructural modification includes the phase change from pearlite to a mixture of martensite and retained austenite. A rapid decrease of hardness occurs between the transformed and the unaltered regions, indicating the existence of a partially transformed region. In samples C and D, the same trend as in sample B can be observed, but their hardened depths decrease to 500 and 200 μm, respectively, as shown in Figure 5(b). The maximum hardness and the hardened depth of each sample are shown in Table II.

E. *Wear Resistance*

Figure 6 shows the wear-test results of the irradiated samples. The evaluation was based on the weight loss after the wear test for sample B through D, as compared to that of the unirradiated sample. Sample A was not tested here, because it did not meet with the objective of the present study to use samples without further machining after irradiation. The irradiated samples have better wear resistance than the unirradiated one. The hardness and wear resistance of the irradiated samples are greatly improved by increasing the input-energy density and the layer depth. This wear resistance indicates a three- or fourfold enhancement and, thus, matches well with the hardness results of Figure 5(b).

F. *Microstructure of Samples Subjected to Thermal Simulation*

Figures 7(a) through (e) are optical micrographs of the thermally simulated samples, which were subjected to abrupt heating at T_p values of 700 °C, 800 °C, 900 °C, 1000 °C, and 1130 °C, respectively, and then quenched. At a T_p lower than 800 °C, no microstructural changes are observed because flake graphites and steadites (marked by arrows) remain in the pearlitic matrix, as can be seen in Figures 7(a) and (b). Although the A_3 transformation temperature is about 723 °C, it can rise upon abrupt heating.[5,26,27] Accordingly, at a fast heating rate (about 100 °C/s), the Ac_3 transformation temperature might rise over 800 °C, thereby causing no phase transformation under 800 °C. When T_p is 900 °C, only the matrix is transformed to fine plate martensite, leaving flake graphites and steadites undissolved (Figure 7(c)). When T_p reaches 1000 °C, martensitic transformation in the matrix occurs overall, but steadites are not found because they are all decomposed (Figure 7(d)). In the case of T_p = 1130 °C, flake graphites remain, plate martensite becomes coarse, and retained austenite starts appearing, as displayed in white in Figure 7(e).

Figures 8(a) through (c) are optical micrographs taken when T_p was raised to the melting point of 1160 °C. Somewhat different structures can be observed, depending on the location. This is because there is some difference in T_p due to local inhomogeneity during heating and cooling. Figure 8(a) shows the formation of a ledeburite eutectic structure due to complete melting. On the other hand, Figure 8(b) shows a mixture of dissolved flake graphites, ledeburite, plate martensite, and retained austenite due to incomplete melting. Around the dissolved flake graphites, a large amount of ledeburite is formed, whereas, in the region far from them, coarse plate martensite and a considerable amount of retrained austenite tend to be formed. Figure 8(c) shows the unmelted region, where flake graphites are partially dissolved while maintaining their forms.

IV. DISCUSSION

When the gray cast iron is irradiated by a high-energy electron beam, the microstructure is modified according to the input-energy density. With a very small input-energy density, the effect of the temperature rise on the microstructural change is negligible, whereas, with a very large input-energy density, the surface layer may melt due to an extreme temperature rise. Thus, the optimum input-energy density conditions should be obtained from investigations based on the thermal history.

The depth of the hardened layer increases with an increasing input-energy density, as shown in Table II, and is graphed in Figure 9. It is almost linearly proportional to the input-energy density. If this relation is extrapolated to the initiation of hardening, it can be found that an input-energy density above 1.1 kJ/cm^2 is required to harden the surface by electron-beam irradiation. By applying this relation between the

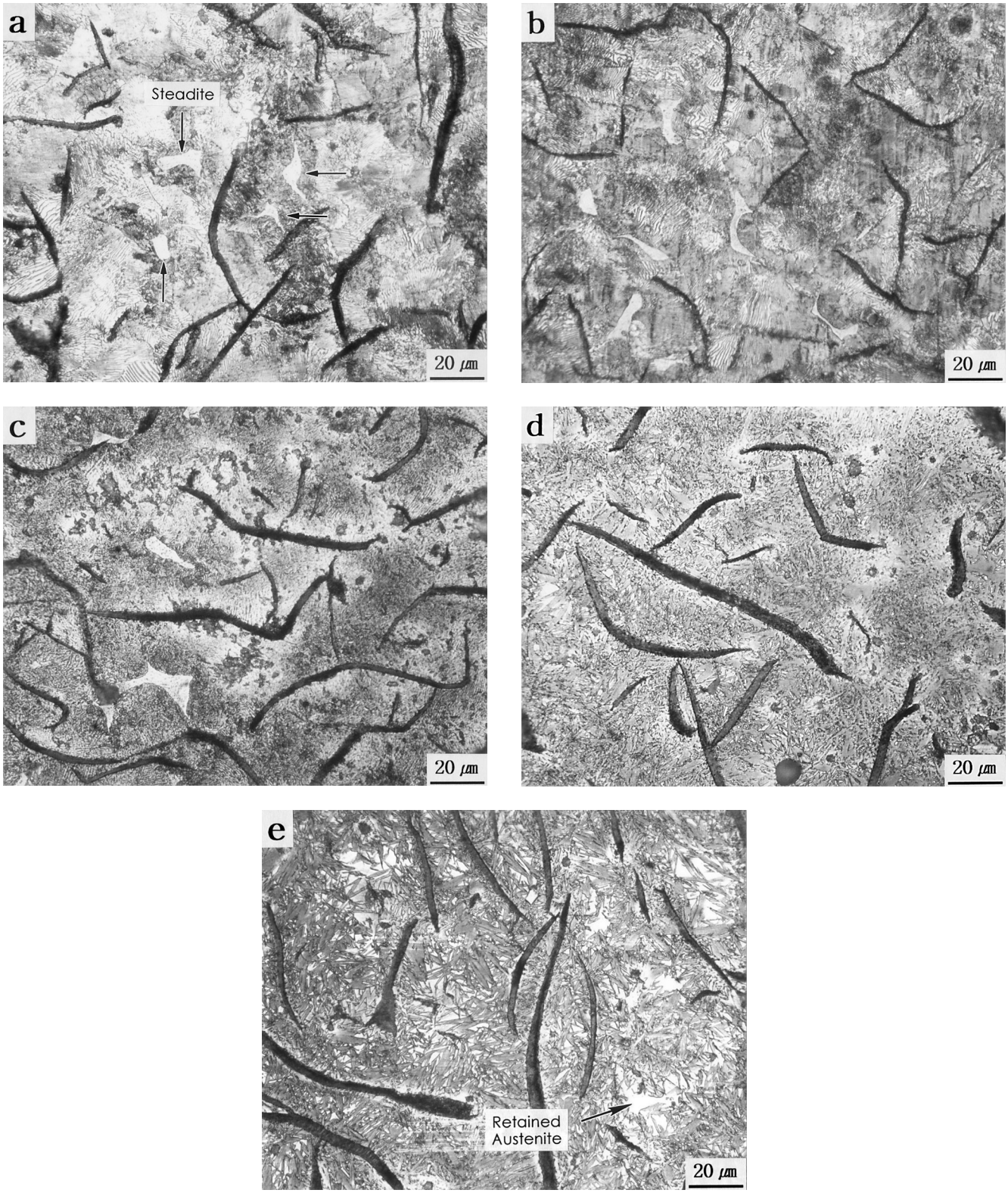

Fig. 7—Optical micrographs of the gray cast iron samples thermally simulated at the peak temperatures (T_p's) of (*a*) 700 °C, (*b*) 800 °C, (*c*) 900 °C, (*d*) 1000 °C, and (*e*) 1130 °C.

input-energy density and the hardened depth, the microstructure and the hardened depth can be controlled.

An understanding of the heat-transfer and phase transformation processes upon irradiation is essential in establishing the optimum microstructure and the process parameters. Since flake graphites and the pearlitic matrix have different thermal properties, the process of heat transfer displays a complex mode. Due to the lack of time for carbon atoms to be sufficiently diffused during the thermal cycle of abrupt heating and cooling, the local inhomogeneity of the carbon

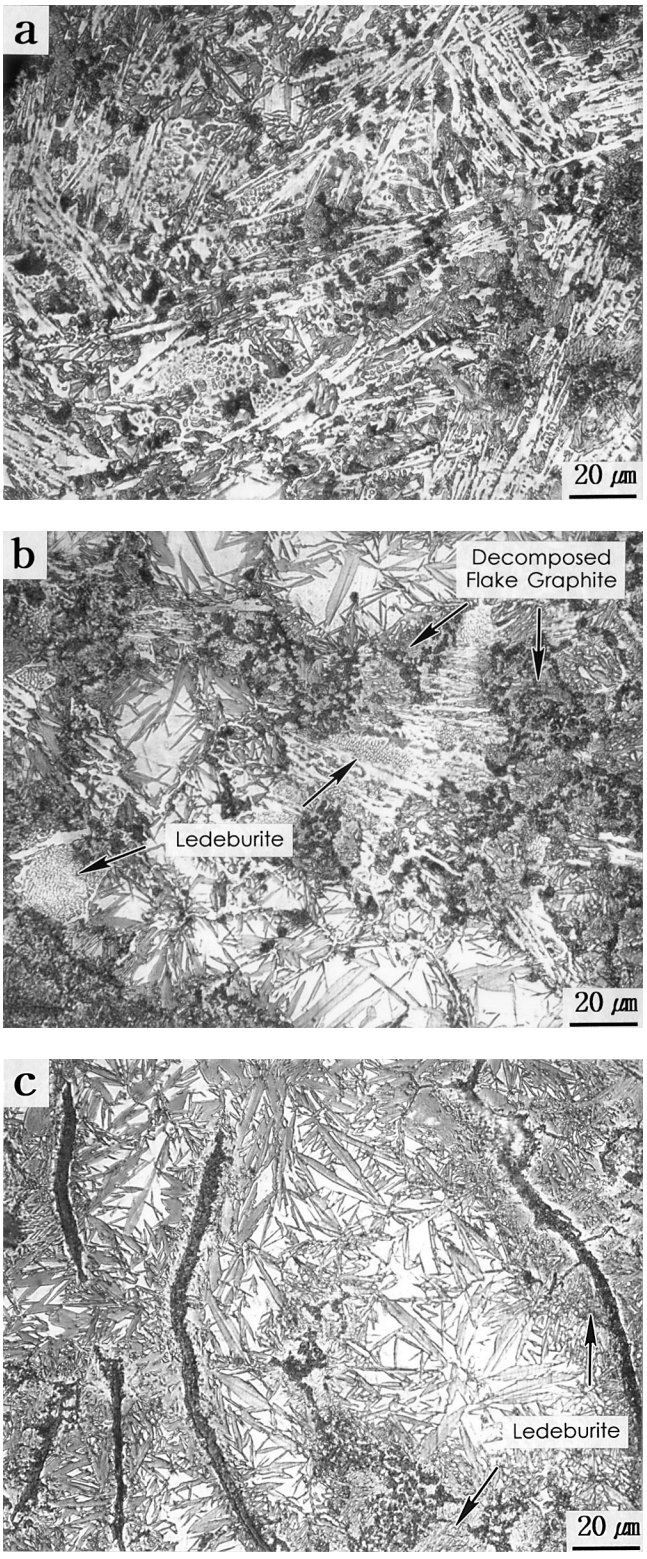

Fig. 8—Optical micrographs of the gray cast iron samples thermally simulated at the peak temperatures (T_p) of 1160 °C, showing (*a*) the ledeburite formation in the completely melted region; (*b*) the complicatedly mixed microstructure containing dissolved flake graphites, ledeburite, plate martensite, and retained austenite in the partially melted region; and (*c*) the dissolution of flake graphites in the martensitic matrix in the transformed region.

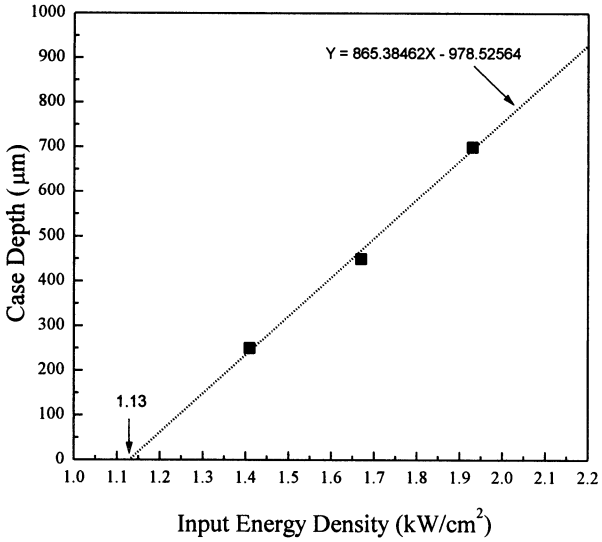

Fig. 9—Hardened case depth *vs* input energy density, showing that minimum input energy density required for the case hardening of the gray cast iron irradiated with high-energy electron beam is about 1.1 kJ/cm^2.

content affects the phase transformation process to a great extent.

To understand the mechanism of microstructural modification upon irradiation, information on input-energy density and the peak temperature is most essential. The application of the following thermal-transfer model is useful in the interpretation of the effects of the process conditions on the microstructural changes. The temperature variation as a function of the depth and the time of irradiation can be calculated using the following equation,[28] taking into consideration the beam-current density, material constants, and process parameters:

$$\frac{\partial T}{\partial t} = K \frac{\partial^2 T}{\partial x^2} + \frac{(1 - f)J(r)}{S} F\left(\frac{x}{S}\right) \qquad [5]$$

where k refers to the thermal conductivity, f is the electron reflectivity on the material surface, S is the electron range, and $J(r)$ is the beam-current density along the distance from the central axis (r) The second column on the right-hand side of Eq. [5] shows the power of the absorbed electron beam per unit area. The term $F(x/S)$ is a geometrical factor indicating the change of heat source with the depth and is expressed in terms of the ratio of S to depth (x), as follows:

$$F\left(\frac{x}{S}\right) = 0.74 + 4.7\left(\frac{x}{S}\right) - 8.9\left(\frac{x}{S}\right)^2 + 3.5\left(\frac{x}{S}\right)^3 \qquad [6]$$

Equation [6] assumes that the heat input is dissipated only by heat conduction through the material itself *via* self-quenching, without considering heat convection.

Because of the complexity of solving nonlinear secondary differential equations like Eq. [5] by an analytical procedure, a finite-difference method, specifically, the implicit method of backward difference, is used. This method provides stable values irrespective of the mesh size.[29] Assumptions were made that the initial condition, *i.e.*, the sample temperature before irradiation, is constant at 20 °C and that there is no heat dissipation due to either radiation or convection on both the surface and the bottom of the sample. These assumptions on

Table IV. Calculated Peak Temperatures from the Thermal Transfer Model (Equation [5])

Sample	Beam Current, I (mA)	Beam Power, P (kW)	Input Energy Density, W (kJ/cm^2)	Calculated Peak Temperature, T_p (°C)
A	8.35	11.7	2.19	1290
B	7.35	10.3	1.93	1138
C	6.35	8.9	1.67	986
D	5.35	7.5	1.41	834
E	4.35	6.1	1.14	687

the boundary conditions were made because there is no time available for irradiated heat input to dissipate on the surface and bottom boundaries, due to the rapid heat transfer into the interior. The assumptions can be expressed as follows.

$$\text{Initial condition: } T(x, 0) = 20\ ^\circ\text{C}$$
$$\text{Boundary condition: } \frac{\partial\, T(x, t)}{\partial x} = 0 \text{ at } x = 0 \text{ and } x = 1.9 \qquad [7]$$

Here, 1.9 refers to the sample thickness. The peak temperatures calculated in the aforementioned manner are listed in Table IV, and the temperature variations *vs* the time and the depth from the surface are graphed in Figures 10(a) and (b). The surface temperature abruptly reaches T_p in 1 second and then rapidly drops to about 300 °C in 4 to 6 seconds due to the rapid cooling by the self-quenching of the material itself (Figure 10(a)). This tendency is common to all samples, with the temperature variation in T_p depending on the input-energy density. In the case of sample A, T_p is 1290 °C, which is higher than the melting point, thereby causing melting. The T_p values of samples B through D are calculated as 1138 °C, 986 °C, and 834 °C, respectively, causing martensitic transformation. In sample E, irradiated with 1.14 kJ/cm^2, microstructural change does not take place, with the calculated T_p being 687 °C. Figure 10(b) illustrates the temperature variation along the depth at T_p and shows a decreasing temperature proportional to the depth beyond 640 μm, which is the electron range. These T_p values correspond well to the microstructural modification of the actually irradiated samples. These findings also confirm the usefulness of the thermal-transfer model in understanding the microstructural modifications.

The thermal-analysis data can be related to those of the thermal simulation test. When T_p is lower than 800 °C, no microstructural modification arises (Figures 7(a) and (b)), indicating that the Ac_3 transformation temperature is above 800 °C. Interpreting this in terms of the microstructural modification in sample D (T_p = 834 °C), where martensitic transformation has occurred, it is found that the Ac_3 transformation temperature lies somewhere between 800 °C and 834 °C. When T_p is 900 °C, the matrix is transformed to martensite, but steadites remain. When it rises to 1000 °C, steadites disappear (Figure 7(d)). This is congruent with the report on the dissolution of steadites at the temperature range from 954 °C to 980 °C.[3] As T_p increases to 1130 °C, plate martensite becomes coarser with increasing amounts of retained austenite, and flake graphites start dissolving. At 1160 °C, close to the melting point, a complex microstructure, composed of the melted region with ledeburite, the partially melted region, with ledeburite, martensite, austenite, and dissolved flake graphites, and the transformed region, is formed. The thermally simulated microstructures match well with those of the actually irradiated samples. However, in the thermally simulated samples, partially dissolved flake graphites exist near the melting point. This discrepancy is associated with the difference in holding time at T_p; 1 second in irradiation *vs* 3 to 4 seconds in thermal simulation. The heat input must have been larger in the latter case. The time held at the austenite temperature region is also extended, which activates the carbon diffusion and the graphite dissolution (Figures 8(b) and (c)).

The thermal analysis results *via* the thermal-transfer model and the thermal simulation test are quite consistent

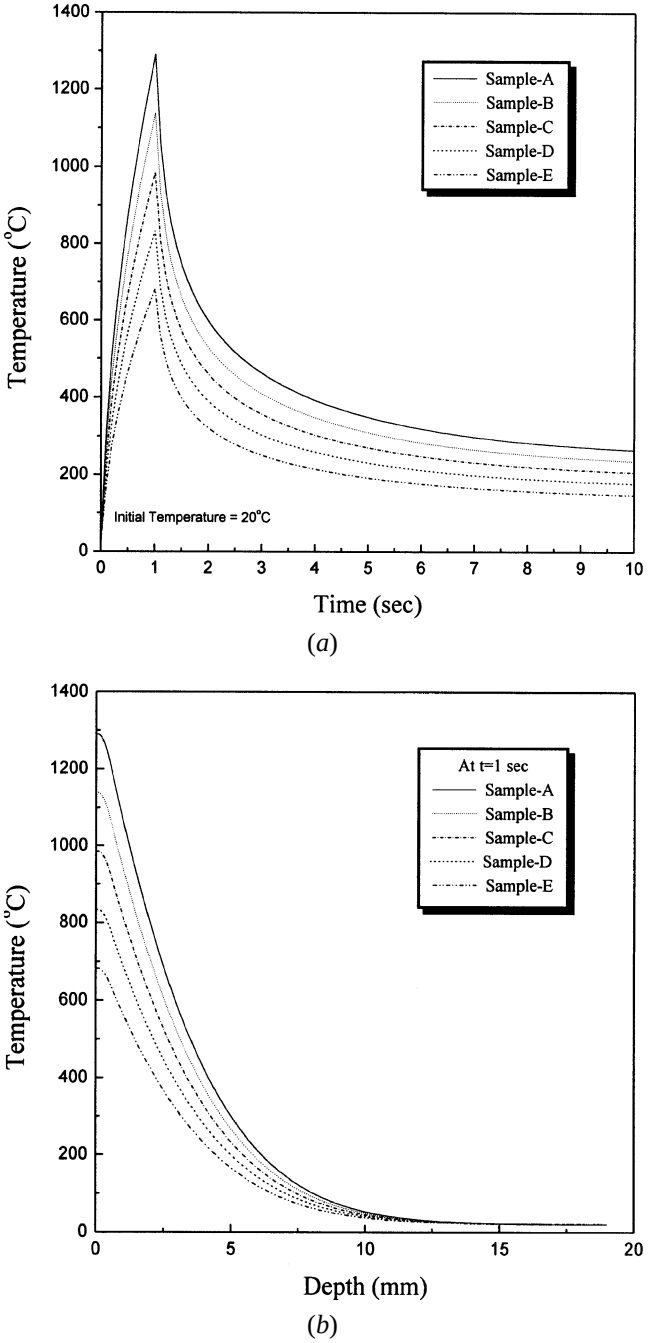

Fig. 10—Temperature variations as a function of (*a*) time and (*b*) depth from the surface for samples A through E irradiated with high-energy electron beam.

with microstructural observations of the irradiated samples and prove to be very significant in clarifying the temperature variation and phase transformation in the process of thermal transfer. For a more-accurate thermal analysis, however, the latent heat accompanying phase transformation and heat convection within the melting pool should be taken into consideration. Since the thermal properties of the gray cast iron are different in flake graphites and in the pearlitic matrix, their respective characteristics should also be considered.

The results of this study provide important experimental data which illuminate the mechanisms of phase transformation, melting, and solidification upon irradiation. In cases where high wear resistance is demanded, not only is the surface hardness greatly improved by the martensitic transformation, but the wear resistance of engine parts is also enhanced to a great extent by controlling the hardened case depth. If the input-energy density is high, as in sample A, the melted-surface region is changed to a white cast iron with high hardness and about 2 mm of the surface layer is hardened. However, in this case, the surface inhomogeneity arising from surface melting requires further machining. When surface hardening is achieved by martensitic transformation without surface melting by using a lower input-energy density, as in sample B, the hardened case depth is about 1 mm. Because of the unoxidized uniform surface, it can be used as a finished product without additional machining.

V. CONCLUSIONS

Based on investigations of the microstructure and wear properties of gray cast iron irradiated by a high-energy electron beam, the following conclusions can be summarized.

1. When the gray cast iron is irradiated with a high-input-energy density, the surface layer is melted and changed into a mixture of ledeburite eutectic structure, retained austenite, and martensite, as in the case of a white cast iron, as the temperature on the irradiated surface layer rises over the melting point and then rapidly cools.

2. The transformed region adjacent to the melted region consists of plate martensite and a considerable amount of retained austenite. As it gets into the interior, plate martensite is refined. In the lower part of this transformed region exists the partially transformed region, where undecomposed cementite lamellae are partially observed.

3. The irradiated surface is hardened by a microstructural modification close to that of white cast iron and by the martensitic transformation. As it gets further into the interior of the transformed region, plate martensite becomes finer and more densely populated and the amount of retained austenite is reduced, resulting in the increase in hardness. The maximum hardness and the hardened depth increase linearly with the input-energy density, with an accompanying improvement in wear resistance.

4. According to the thermal simulation test results, ledeburite is formed when the peak temperature rises over the melting point, whereas the pearlitic matrix is transformed into plate martensite when it rises over the austenite-temperature region. The amount of retained austenite increases and flake graphites tend to be dissolved by increasing the peak temperature. The thermal analyses through the thermal-transfer model and the thermal simulation test are quite congruent with the microstructural analyses of the actually irradiated samples, confirming the usefulness of these thermal analyses in the interpretation of microstructural modification.

ACKNOWLEDGMENTS

This work was supported by the 1996 Ministry of Education Research Fund for Advanced Materials and Kia Motors Corp. The authors thank Professors Nack J. Kim and Yangmo Koo and Dr. Dongwoo Suh, POSTECH, and Drs. Won Suk Cho and Sang Ho Kim and Mr. Sung Mu Choi, Kia Motors Corp., for their helpful discussion on microstructural analysis. Use of the electron accelerator of the Budker Institute of Nuclear Physics is also gratefully acknowledged.

REFERENCES

1. H.T. Angus: *Cast Iron; Physical and Engineering Properties*, 2nd ed., Butterworth and Co., London, 1976, pp. 161-76.
2. R. Elliott: *Cast Iron Technology*, Butterworth and Co., London, 1988, ch. 1.
3. W.F. Smith: *Structure and Properties of Engineering Alloys*, 2nd ed., McGraw-Hill, Inc., New York, NY, 1993, ch. 8.
4. I. Minkoff: *The Physical Metallurgy of Cast Iron*, John Wiley & Sons, Ltd., New York, NY, 1983, ch. 3.
5. N. Zárubová, V. Kraus, and J. Čermák: *J. Mater. Sci.*, 1992; vol. 27, pp. 3487-96.
6. C.H. Chen, C.J. Altstetter, and J.M. Rigsbee: *Metall. Trans. A*, 1984, vol. 15A, pp. 719-28.
7. F. Fouquet and E. Szmatula: *Mater. Sci. Eng.*, 1988, vol. 98, pp. 305-08.
8. C.W. Draper and P. Mazzoldi: *Laser Surface Treatment of Metals*, NATO ASI Series E, No. 115, NATO, Martinus Nijhoff, Boston, 1986, pp. 413-33.
9. I.L. Pobol': *Met. Sci. Heat Treatment*, 1991, vol. 32 (7–8), pp. 520-27.
10. I. Atsushi: *Bull. Jpn. Soc. Prec. Eng.*, 1984, vol. 18 (3), pp. 219-24.
11. D.N.H. Trafford, T. Bell, J.H.P.C. Megaw, and A.S. Bransden: *Met. Technol.*, 1983, vol. 10, pp. 69-77.
12. K.G. Budinski: *Surface Engineering for Wear Resistance*, Prentice-Hall, Englewood Cliffs, NJ, 1988, ch. 7.
13. J.M. Poate, G. Foti, and D.C. Jacobson: *Surface Modification and Alloying by Laser, Ion, and Electron Beams*, NATO Conf. Proc. Series VI, Plenum Press, New York, NY, 1983, vol. 8, ch. 1.
14. A.F. Baisman, S.B. Vasserman, M.G. Golkovskii, V.D. Kedo, and R.A. Salimov: *About Surface Hardening by Concentrated Electron Beam at Atmosphere*, Preprint No. 88-73, Budker Institute of Nuclear Physics, Novosibrsk, Russia, 1988, pp. 5-31.
15. D. Suh, S. Lee, Y. Koo, and H.C. Lee: *Metall. Mater. Trans. A*, 1996, vol. 27A, pp. 3149-61.
16. D. Suh, S. Lee, and Y. Koo: *Metall. Mater. Trans. A*, 1997, vol. 28A, pp. 637-47.
17. S. Schiller, U. Heisig, and S. Panzer: *Electron Beam Technology*, John Wiley & Sons, Ltd., New York, NY, 1982, ch. 2.
18. T. Tabata and R. Ito: *Nucl. Sci. Eng.*, 1974, vol. 55, pp. 226-39.
19. S. Schiller, U. Heisig, and S. Panzer: *Electron Beam Technology*, John Wiley & Sons, Ltd., New York, NY, 1982, ch. 1.
20. S. Schiller, U. Heisig, and S. Panzer: *Electron Beam Technology*, John Wiley & Sons, Ltd., New York, NY, 1982, ch. 7.
21. R. Ito, P. Andreo, and T. Tabata: *Radiat. Phys. Chem.*, 1993, vol. 42, pp. 761-64.
22. R.L. Ingalls: in *Introduction to Mössbauer Spectroscopy*, L. Moy, ed., Plenum Press, New York, NY, 1971, ch. 5.
23. C.F. Walton: *Gray and Ductile Iron Castings Handbook*, Gray and Ductile Iron Founder's Society, Cleveland, OH, 1971, p. 105.
24. W.K. Dalton: *The Technology of Metallurgy*, Macmillan Publishing Co., New York, NY, 1993, ch. 7.
25. M. Hillert and V.V. Subba Rao: *Grey and White Solidification of Cast Iron*, Proc. Solidification of Metals, The Iron and Steel Institute, London, 1968, pp. 204-12.
26. J.R. Bradley and S. Kim: *Metall. Trans. A*, 1988, vol. 19A, pp. 2013-25.
27. M.F. Ashby and K.E. Easterling: *Acta Metall.*, 1984, vol. 32, pp. 1935-48.
28. D. Suh, S. Lee, S.-J. Kwon, and Y.M. Koo: *Metall. Mater. Trans. A*, 1997, vol. 28A, pp. 1499-1508.
29. R.L. Burden and J.D. Faires: *Numerical Analysis*, 5th ed., Prindle, Weber & Schmidt Pub. Co., Boston, MA, 1993, pp. 380-82.